Supplementary Information

Cooperative tungsten centres in a polymetric carbon nitride for the artificial photosynthesis of hydrogen peroxide

Chengyang Feng[a], Jun Luo[b], Cailing Chen[a], Shouwei Zuo[a], Yuanfu Ren[a], Zhipeng Wu[a], Miao Hu[a], Samy Ould-Chikh[a], Javier Ruiz-Martinez[a], Yu Han[a,*], Huabin Zhang[a,*]

[a] KAUST Catalysis Center (KCC), Division of Physical Science and Engineering, King Abdullah University of Science and Technology (KAUST), Thuwal, 23955-6900 Kingdom of Saudi Arabia.

[b] State Key Laboratory of Featured Metal Materials and Life-cycle Safety for Composite Structures, MOE Key Laboratory of New Processing Technology for Nonferrous Metals and Materials, School of Resources, Environment and Materials, Guangxi University, Nanning 530004, China.

Correspondence and requests for materials should be addressed to Y.H. and H.Z. (e-mail: yu.han@kaust.edu.sa; huabin.zhang@kaust.edu.sa)

Experimental section

Preparation of photocatalysts. Unless otherwise stated, all the chemicals used in this work are of analytical grade and commercially available. All the aqueous solutions referred are prepared using deionized water. The pristine PCN was prepared as the following process. 2 g melamine was put into a horizontal tube furnace and heated to 520 °C at a rate of 2.5 °C min^{-1} and maintained at 520 °C for 4 h. After cooling to ambient temperature, the yellow agglomerates (PCN) were obtained and grounded into powder. The CNW samples were prepared by a bottom-up method as follows: a certain amount of WCl_6 (0.05, 0.1, 0.2, 0.3, 0.4, 0.5 mmol) was dissolved in 50 mL of ethanol and kept stirring until the solution is clear. 2g melamine was put into the above solution and stirred for one hour until W^{6+} is completely absorbed. The solvent in the solution was removed by rotatory evaporator and vacuum oven. The obtained white powder was transferred into a tube furnace and heated to 520 °C at a rate of 2.5 °C min^{-1} then kept at 520 °C for 4 h. After the furnace was cooled down naturally to ambient temperature, the CNW samples (recorded as CNW005, CNW01, CNW02, CNW03, CNW04 and CNW05 corresponding to WCl_6 dosage of 0.05, 0.1, 0.2, 0.3, 0.4, 0.5 mmol, respectively) was obtained and grounded into powder for further use.

Characterization. The crystalline phases were characterized by a powder X-ray diffraction instrument (Bruker D8 Advanced A25 diffractometer) with a Cu Kα target (λ = 1.54056 Å) at 40 kV and 40 mA. HAADF-STEM and elemental mapping were performed on a Titan Themis Z microscope. TEM images were obtained on a Titan ST microscope from Thermo Fisher Scientific. SEM was performed on an FEI Teneo VS scanning electron microscopy. The specific surface areas and pore size distribution of samples were determined via N_2 adsorption–desorption and Brunauer–Emmett–Teller (BET) method by a surface area analyzer (Micromeritics ASAP 2020 surface area and porosity

analyzer). FTIR spectra were obtained on a Nicolet iS10 FTIR spectrometer. XPS measurements were performed on an ESCALAB 250Xi spectrometer (Thermo Fisher) with a monochromatic Al Kα X-ray source. The X-ray absorption spectroscopy for the W L-edge was measured at an easyXAFS300 spectrometer. The optical absorption properties of the samples were determined using the diffuse reflection method on a UV-visible light near-infrared spectrometer (Lambda 950). EPR measurements were obtained at room temperature using a Bruker EMX-10/12 EPR spectrometer operated in the X-band frequency. Steady-state PL spectra were recorded on a Carry Eclipse fluorescence spectrometer. Time-resolved PL decay curves were obtained on FLS980 fluorescence spectrometers. In situ DRIFT spectra measurements were performed on a Nicolet 6700 Harrick spectrometer with an MCT detector. Raman spectroscopy was performed on an RXN1 Raman spectrometer (Kaiser Optical Systems). The zeta-potential data were obtained on a Zetasizer Nano ZS90.

X-ray absorption fine structure experiments: The X-ray absorption spectroscopy (XAS) for the W L-edge was measured at an easyXAFS300 spectrometer. W foils were detected in the transmission mode to serve as the reference for energy calibration. A suitable quantity of the sample was ground, combined with boron nitride (BN), and compacted into pieces with a 10 mm diameter for testing. X-ray absorption near-edge spectroscopy (XANES) and extended X-ray absorption fine structure spectroscopy (EXAFS) were used to study the valence states and coordination environments of samples. The K edge position is determined by the maximum value of the first derivative of the absorbing edge. The data were analyzed using the ATHENA and ARTEMIS (version 0.9.26) modules implemented in the IFEFFIT software packages.[1] EXAFS functions were Fourier transformed to the R space with a k-weight of 2 in the range of 4.17-10.7 $Å^{-1}$ using a hanning windows (dk=1.0 $Å^{-1}$). For W absorption edge, the value of amplitude reduction factor (S_0^2) in this study was found to be 0.795

by fitting standard W foil XAFS data. Two paths [W-N, and W-C] based on the crystal structure were used for fitting the XAFS data. All data were fitted with k-weight of 2 in R space.

Photocatalytic production of H_2O_2. Typically, 10 mg of photocatalyst was dispersed in 100 mL deionized water. The suspended solutions were stirred for 30 min in the dark with continual O_2 bubbling after ultrasound treatment to reach an absorption–desorption equilibrium. Then the solutions were exposed to visible light provided by a 300 W Xe lamp with a 420 nm cutoff filter. The light source was located at a distance of 10 cm from the reactor, and a continuous magnetic stirrer and cooling water were applied during the experiment. During illumination, 3 mL solution was sampled every hour and filtrated with a 0.22 μm to remove the photocatalyst.

The concentration of H_2O_2 was determined by titration methods.[2] The amount of H_2O_2 was first analyzed by iodometry as follows.[3] 1 mL of 0.1 mol L^{-1} $C_8H_5KO_4$ aqueous solution and 1 mL of 0.4 mol L^{-1} potassium iodide (KI) aqueous solution was added to the obtained sample and kept for 30 min. The H_2O_2 molecules reacted with iodide anions (I^-) under acidic conditions ($H_2O_2 + 3I^- + 2H+ \rightarrow I_3^- + 2H_2O$) to produce triiodide anions (I_3^-) possessing a strong absorption at around 350 nm. The amount of I_3^- was determined by means of UV–vis spectroscopy, from which the amount of H_2O_2 produced during each reaction was estimated (Fig. S15). To validate the achieved yields and enhance the precision of the reported specifications, we double-checked the H_2O_2 concentration using a colorimetric method reliant on cerium sulfate titration ($2Ce^{4+} + H_2O_2 \rightarrow 2Ce^{3+} + 2H^+ + O_2$).[4] Fig. S16 displayed the linear fitting of absorbance and H_2O_2 concentration, demonstrating the exceptional detection sensitivity achieved.

The rate constants for H_2O_2 formation (K_f) and decomposition (K_d) over prepared catalysts were evaluated by assuming zero-order and first-order kinetics, respectively. Values of K_f and K_d are

obtained by fitting the H_2O_2 evolution data to the following equation:

$$[H_2O_2] = \frac{k_f}{k_d}\{1 - \exp(-k_d t)\}$$

Determination of apparent quantum yield. The apparent quantum yield (AQY) was determined by a multi-channel photocatalytic reactor (PCX-500C Discover, Perfect Light). The photoreaction was performed in 50 mL deionized water with CNW03 photocatalyst (200 mg) under O_2 atmosphere. The wavelength of incident light is adjusted to 420, 450, 485 and 535nm, respectively. The AQY was calculated by the following formula:

$$AQY = \frac{2 \times n_{H_2O_2}}{n_{photons}} \times 100\%$$

where $n_{H_2O_2}$ is the amount of generated H_2O_2 and $n_{photons}$ is the number of incident photons.

Determination of solar-to-chemical conversion efficiency. The solar-to-chemical conversion efficiency (SCC) was tested in 100 mL deionized water with 500mg CNW03 photocatalyst under AM1.5 global spectrum. A 420 nm cutoff filter was used to avoid the decomposition of H_2O_2 by UV light. The SCC was calculated by the following formula:

$$SCC = \frac{\Delta G_{H_2O_2} \times n_{H_2O_2}}{t_{ir} \times S_{ir} \times I_{AM}} \times 100\%$$

where $\Delta G_{H_2O_2}$ is the free energy for H_2O_2 formation (117kJ mol^{-1}), $n_{H_2O_2}$ is the amount of generated H_2O_2, t_{ir} is the irradiation times, S_{ir} is the irradiation area. I_{AM} is the overall irradiation intensity.

Photoelectrochemical characterizations.

A standard three-electrode system was used to conduct the photoelectrochemical characterizations on a CHI760E electrochemical workstation, with a Pt electrode and an Ag/AgCl electrode as the counter and reference electrode, respectively. An FTO (active area of 1 cm^2) electrode covered with samples was used as the working electrode. A 300 W Xe lamp was used as the light source. A rotating ring-

disk electrode (RRDE) was used to evaluate the number of transferred electrons (n) and H_2O_2 selectivity in the ORR reaction. The RRDE tests were conducted in an O_2-saturated 0.1M KOH solution with a rotating speed of 1600 rpm. The number of transferred electrons (n) is calculated according to the following formula:

$$n = 4 \times \frac{I_d}{I_d + I_r/N}$$

The selectivity of H_2O_2 is calculated by the following formula:

$$H_2O_2\% = 200 \times \frac{I_r/N}{I_d + I_r/N} \times 100\%$$

where I_r is the ring current, I_d is the disc current, and N is the collection efficiency (N = 0.41).

Computational details. Calculations with the CP2K/Quickstep package used periodic boundary conditions for both models.[5] Geometries and energies were carried out using the hybrid Gaussian and plane wave basis set and Goedecker-Teter-Hutter (GTH) pseudopotentials.[6, 7] The optimized lattice parameters were 16.73, 12.71, 15.00 Å, and 90.0, 90.0, and 90.0º, respectively. The DIMER methods were used to optimize the transition state and further confirmed by vibrational frequency analysis.[8] The plane wave cutoff was set to 500 Ry. The Gaussian basis set consisting of a double-ζ with one set of polarisation functions (DZVP) was used to optimize structures.[9] For the energy calculation in reaction pathway, the triple-ζ with one set of polarisation functions (TZVP) basis set was employed. The Perdew-Burke-Ernzerhof exchange-correlation functional[10] with the approach of Grimme (DFT-D3)[11] was adopted. Due to the large size of the model, single gamma point grid sampling was used. The free energies were calculated as $\Delta G = \Delta E + \Delta ZPE - T\Delta S$, where ΔE is the reaction energy, ΔZPE is the zero-point energy change, T is temperature, and ΔS is the entropy difference between the products and the reactants. The pre- and post-processing of the calculation were finished via the

Multiwfn 3.7(dev) code.[12]

Supplemental Figures and Tables

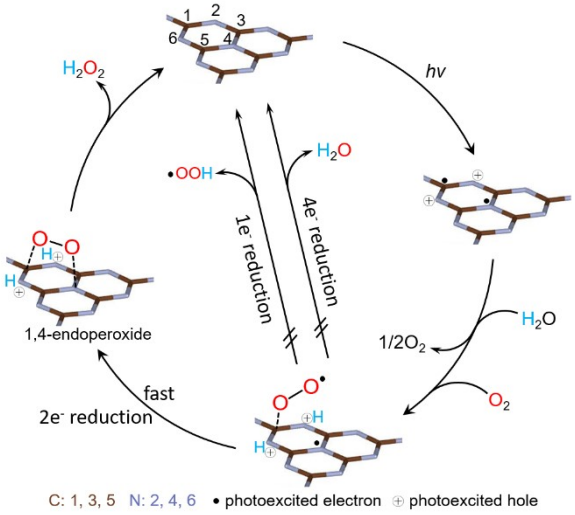

Fig. S1 Proposed mechanism for selective H_2O_2 formation on the surface of polymetric carbon nitride.

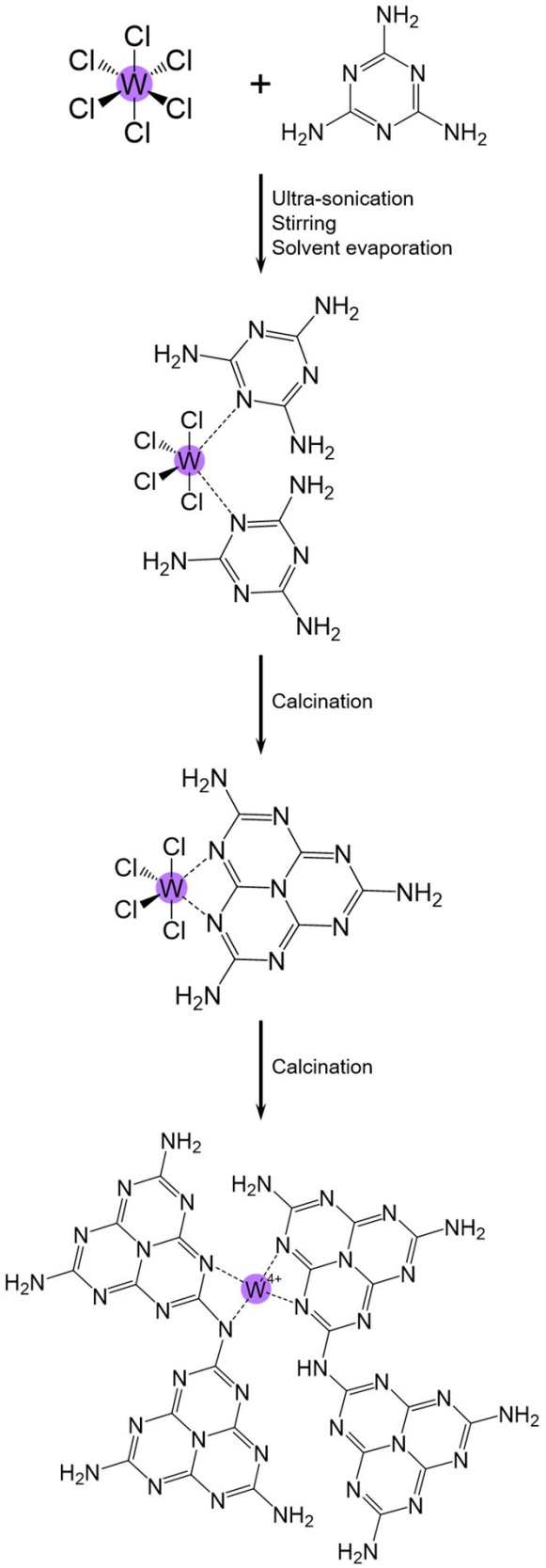

Fig. S2 The preparation procedure of the CNW photocatalyst.

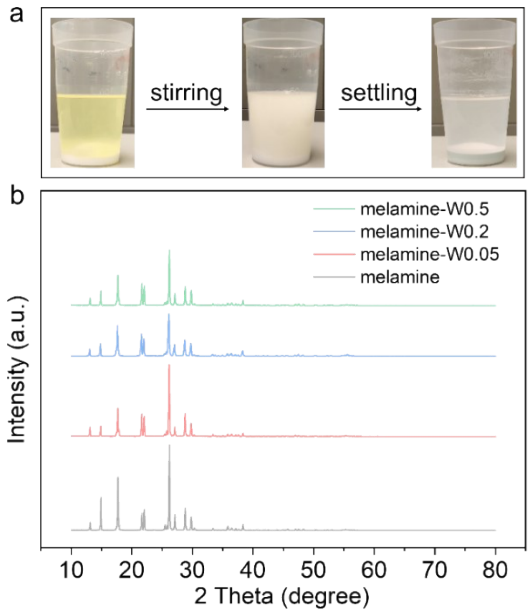

Fig. S3 (a) Digital photographs of the W adsorption process. (b) XRD patterns of the melamine precursor adsorbed with different amounts of W.

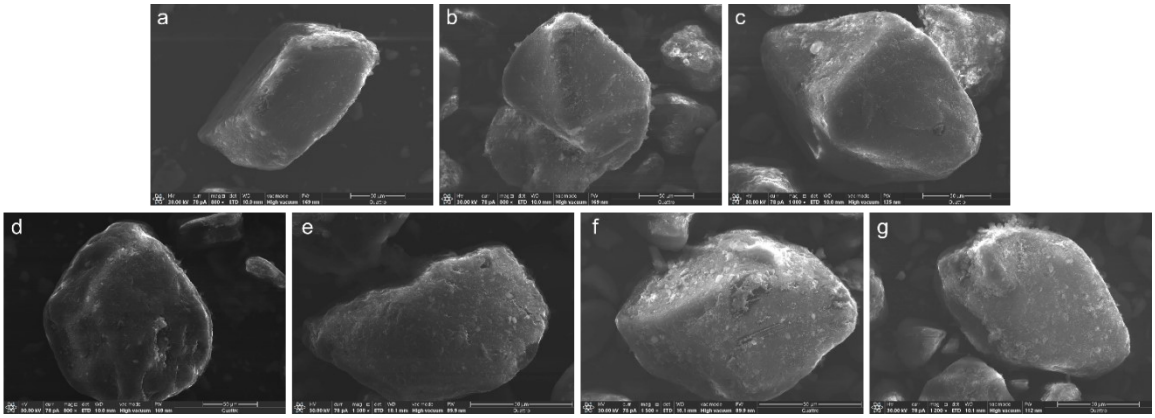

Fig. S4 SEM images of (a) melamine, (b) melamine-W0.05, (c) melamine-W0.1, (d) melamine-W0.2, (e) melamine-W0.3, (f) melamine-W0.4, (g) melamine-W0.5.

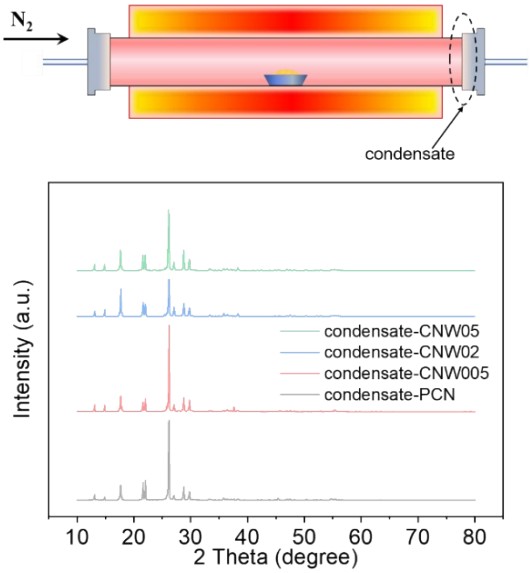

Fig. S5 XRD patterns of the condensed deposits at the outlet of tube furnace.

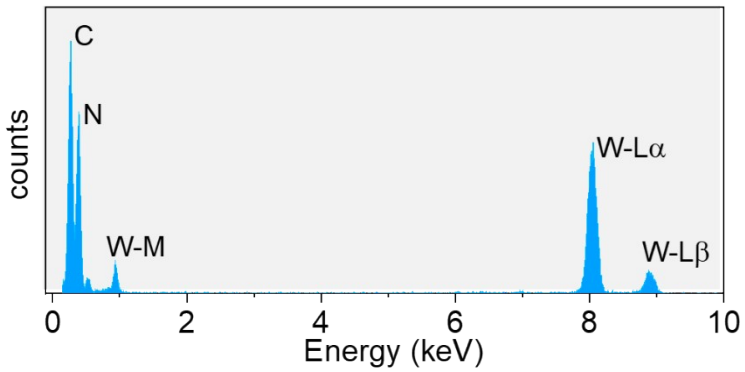

Fig. S6 EDX spectra of CNW03.

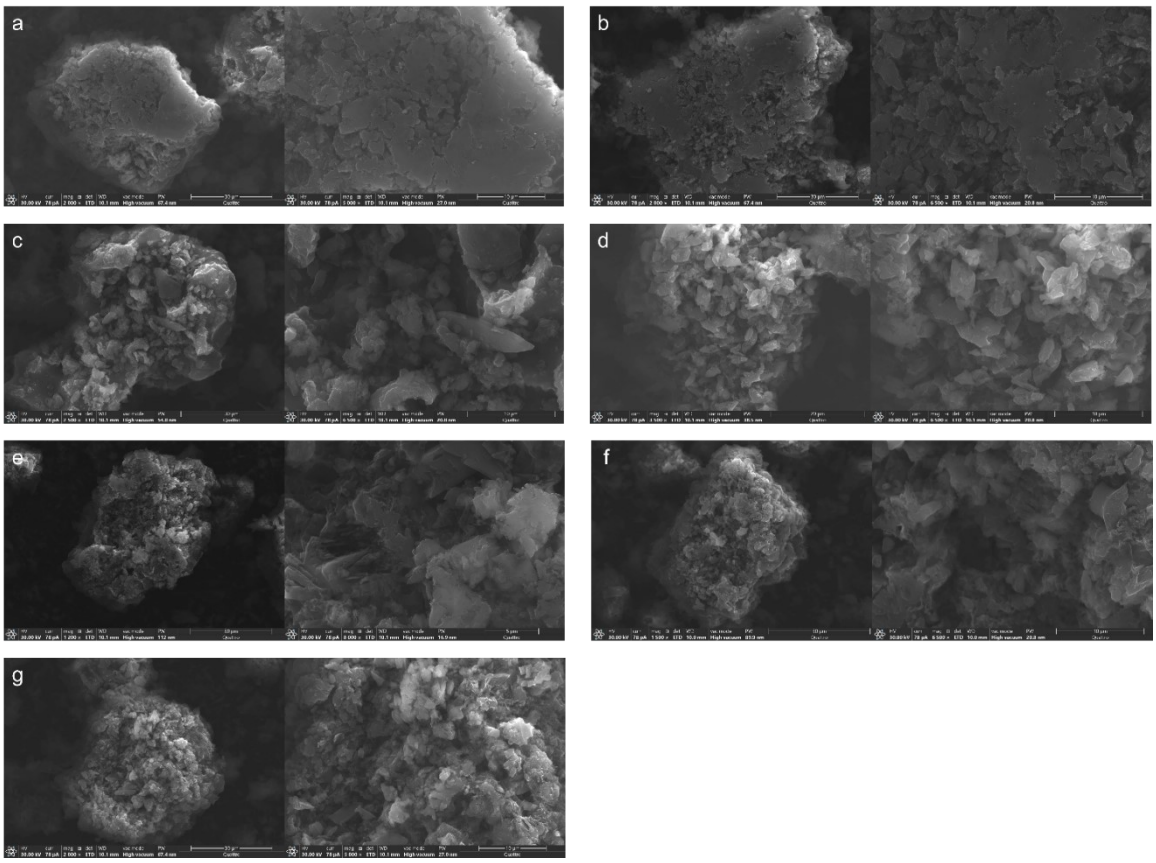

Fig. S7 SEM images of (a) PCN, (b) CNW005, (c) CNW01, (d) CNW02, (e) CNW03, (f) CNW04, (g) CNW05.

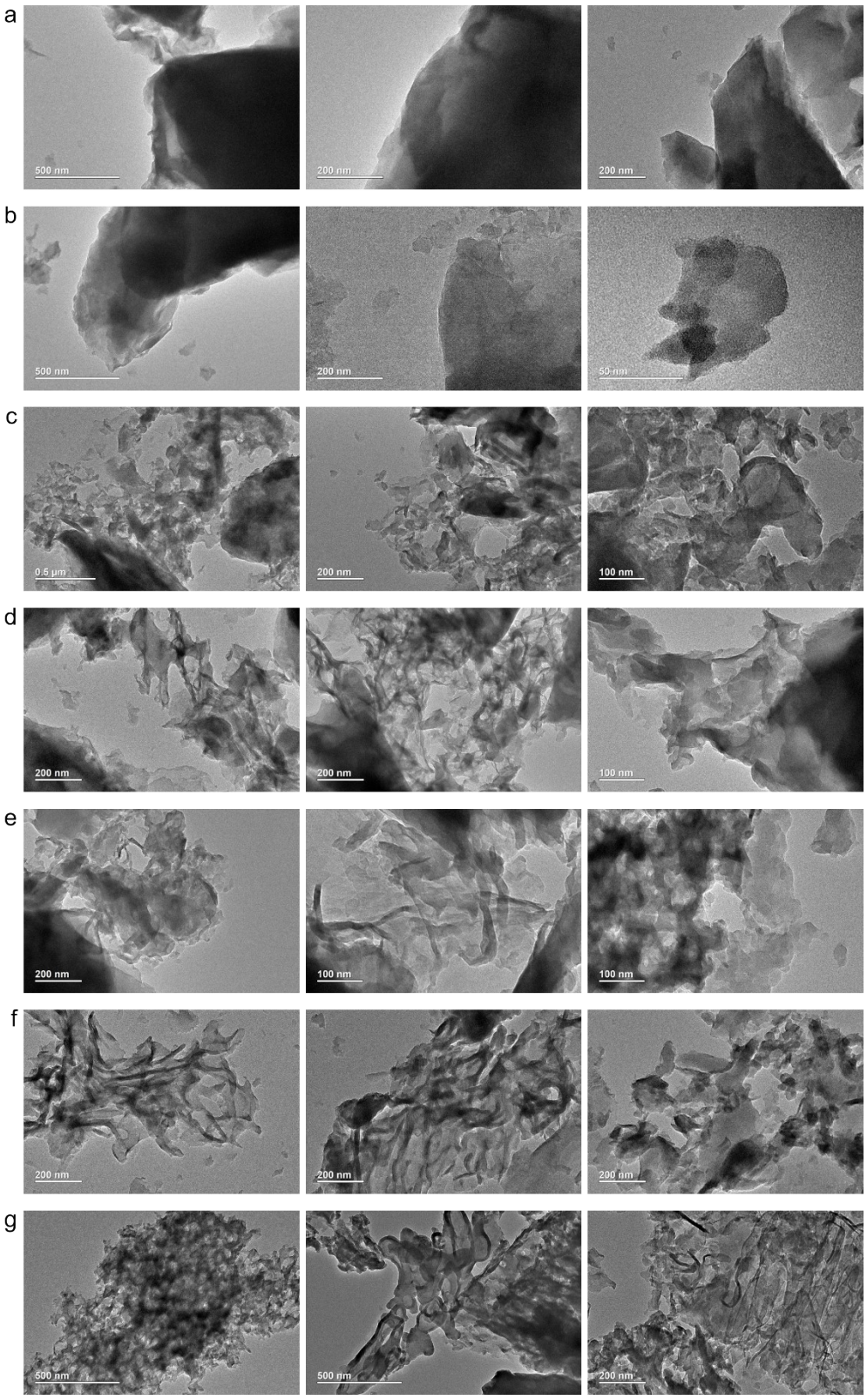

Fig. S8 TEM images of (a) PCN, (b) CNW005, (c) CNW01, (d) CNW02, (e) CNW03, (f) CNW04, (g) CNW05.

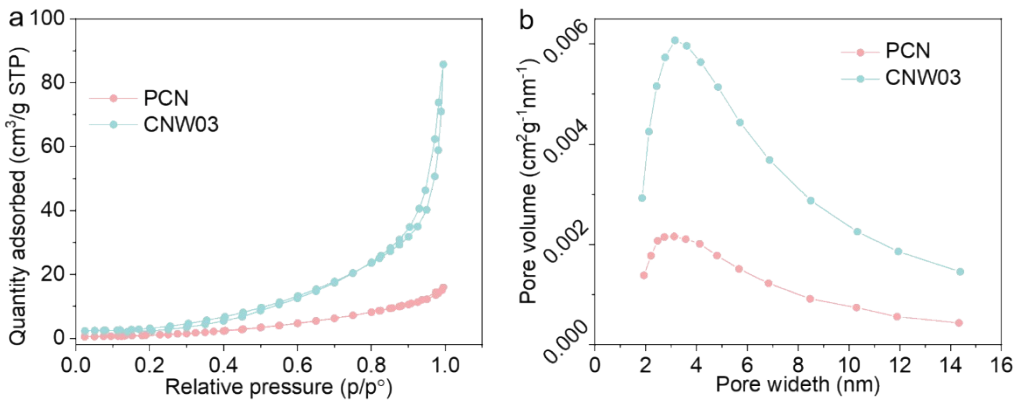

Fig. S9 BET analysis of pristine PCN and CNW03. (a) N_2 adsorption-desorption isotherms. (b) Pore size distribution curves.

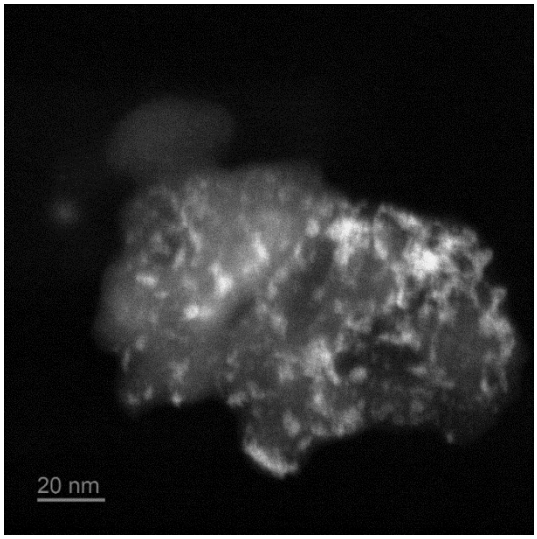

Fig. S10 HAADF-STEM image of CNW05

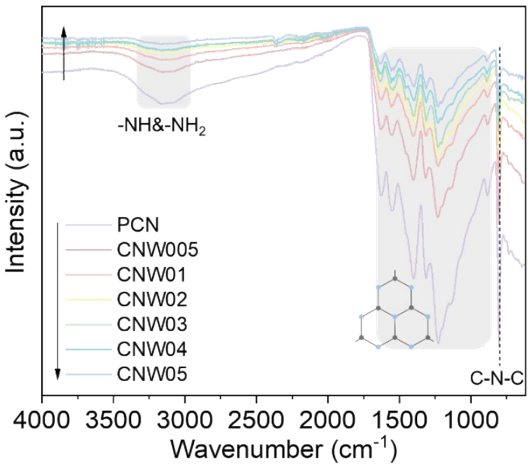

Fig. S11 FTIR spectra of prepared catalysts.

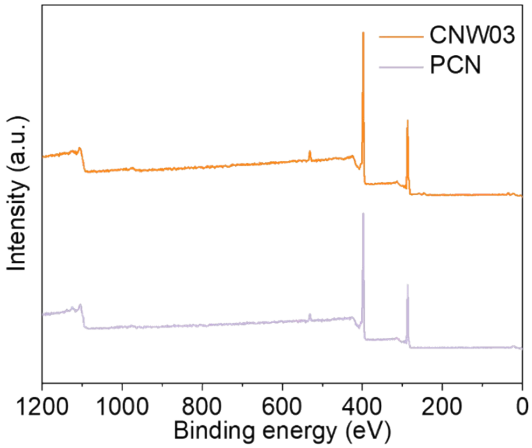

Fig. S12 XPS spectra of prepared catalysts.

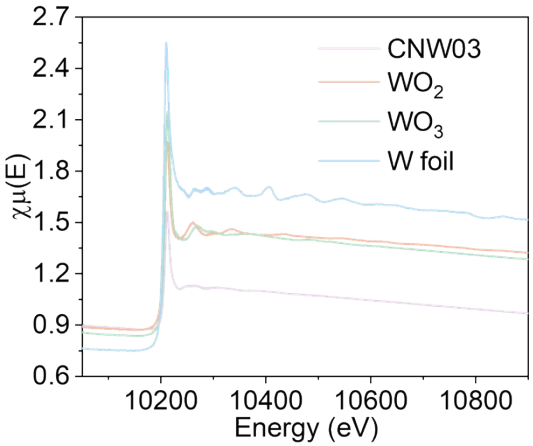

Fig. S13 Original XANES experimental spectra of CNW03, WO_2, WO_3 and W foil.

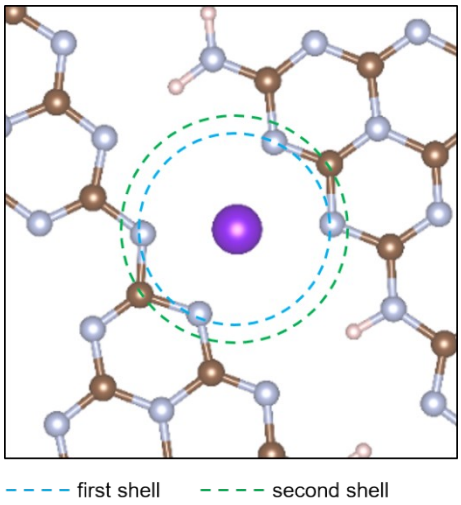

Fig. S14 Schematic description for the coordination shells for the isolated W over the g-C_3N_4.

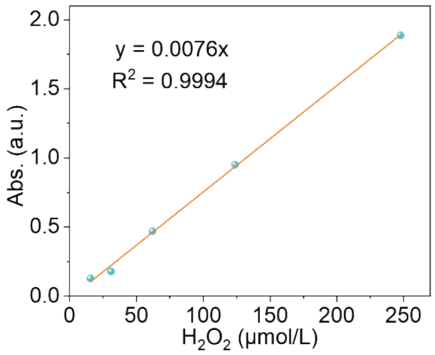

Fig. S15 Iodometry calibration curves of absorbance change as a function of the concentration of H_2O_2.

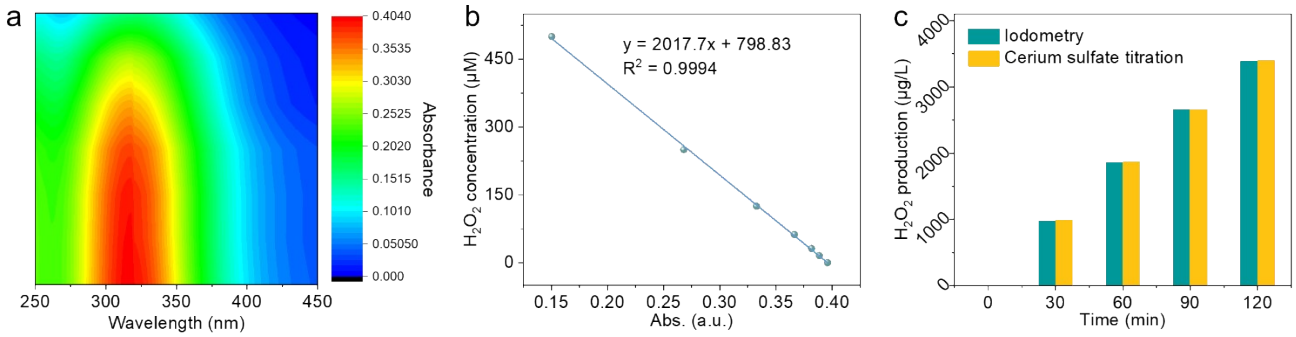

Fig. S16 Colorimetric method calibration. (a) Contour map of UV-vis absorption spectra for cerium titration by known H_2O_2 concentration and (b) liner fitting of absorbance at 320 nm wavelength. (c) Comparison of H_2O_2 concentration during photocatalytic reaction over CNW03 measured using iodometry and cerium sulfate titration methods.

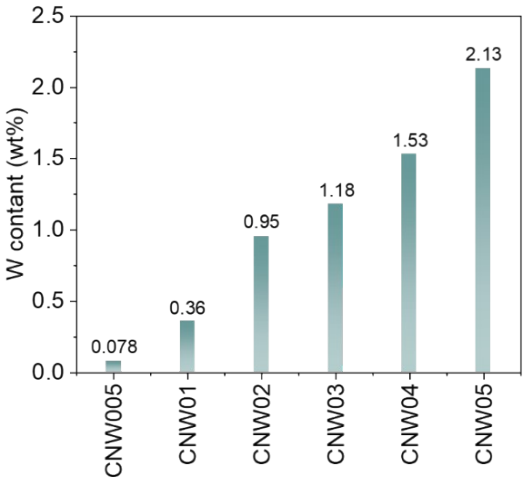

Fig. S17 The loading content obtained by ICP-MS.

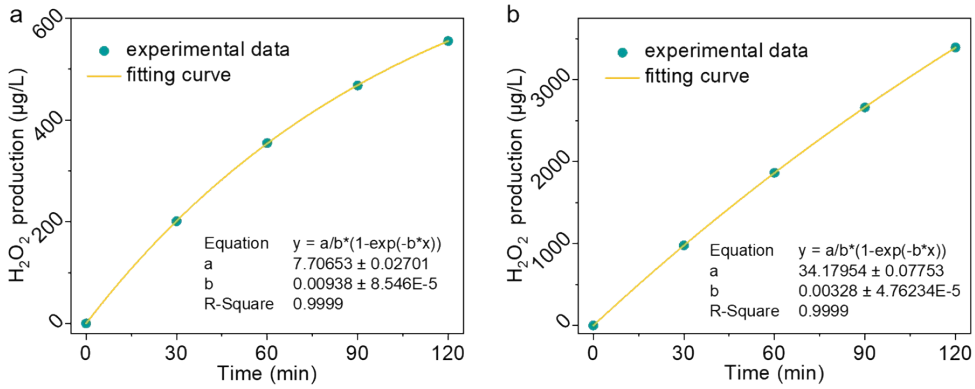

Fig. S18 Kinetic fitting curves of H_2O_2 generation over (a) PCN and (b) CNW03.

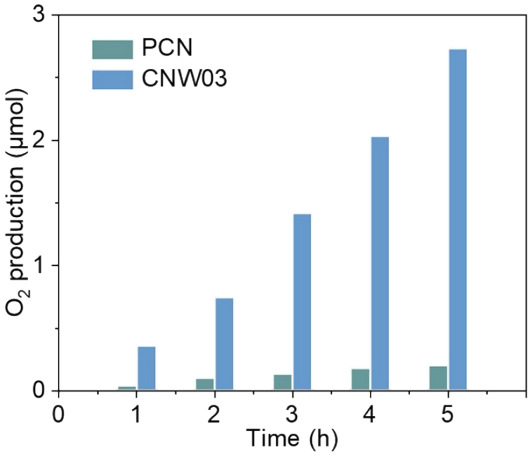

Fig. S19 Photocatalytic O_2 evolution over PCN and CNW03 sample.

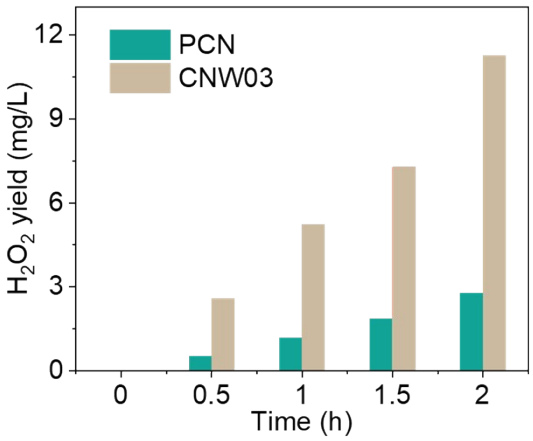

Fig. S20 Photocatalytic H_2O_2 evolution over PCN and CNW03 sample in IPA solution.

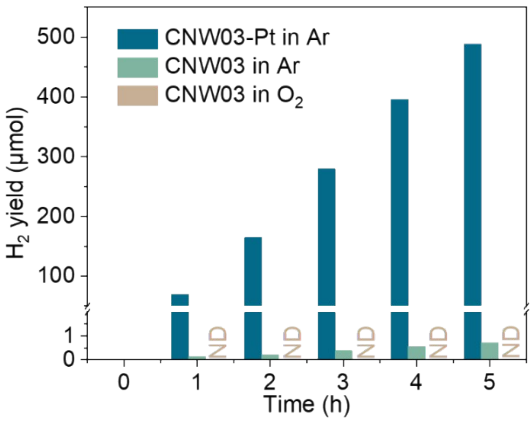

Fig. S21 Photocatalytic H_2 generation over CNW03 under different condition.

Photocatalytic H_2 generation experiments show that the CNW03 sample shows very limited H_2 generation activity without Pt cocatalyst. More importantly, when the reaction system is in an O_2 atmosphere, the hydrogen evolution reaction no longer occurs, indicating that the ORR reaction has higher priority.

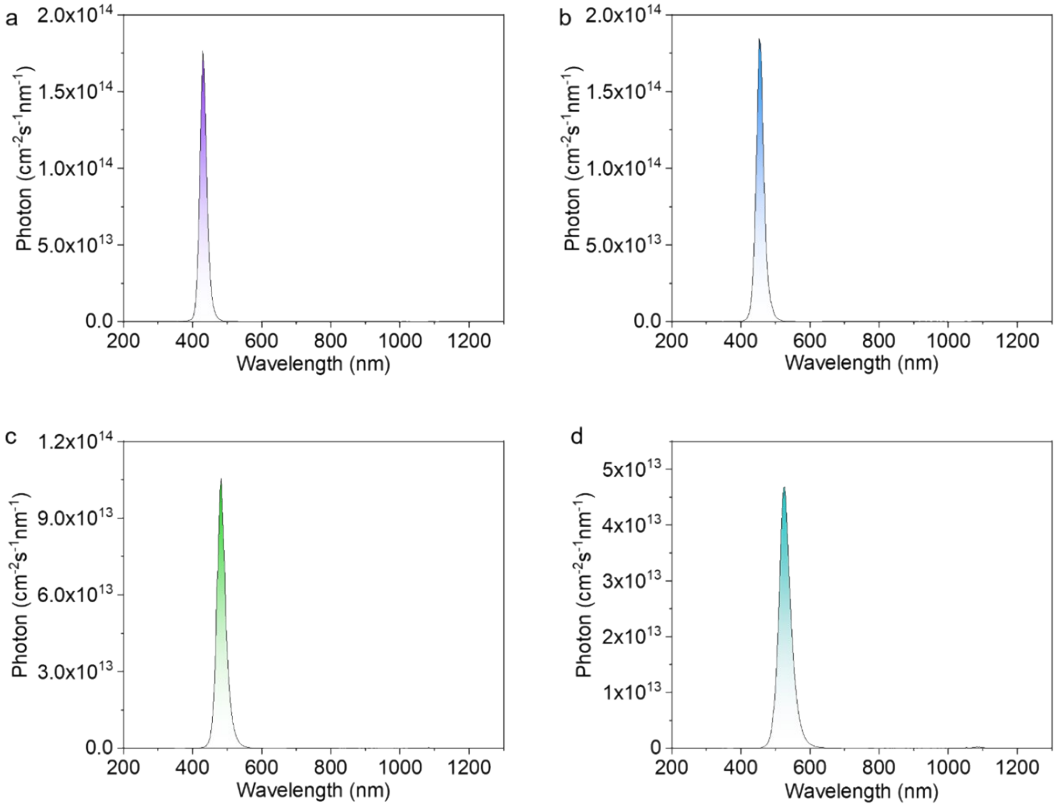

Fig. S22 The irradiance of sources used for AQY testing. (a) 420 nm, (b) 450 nm, (c) 485 nm, (d) 535nm.

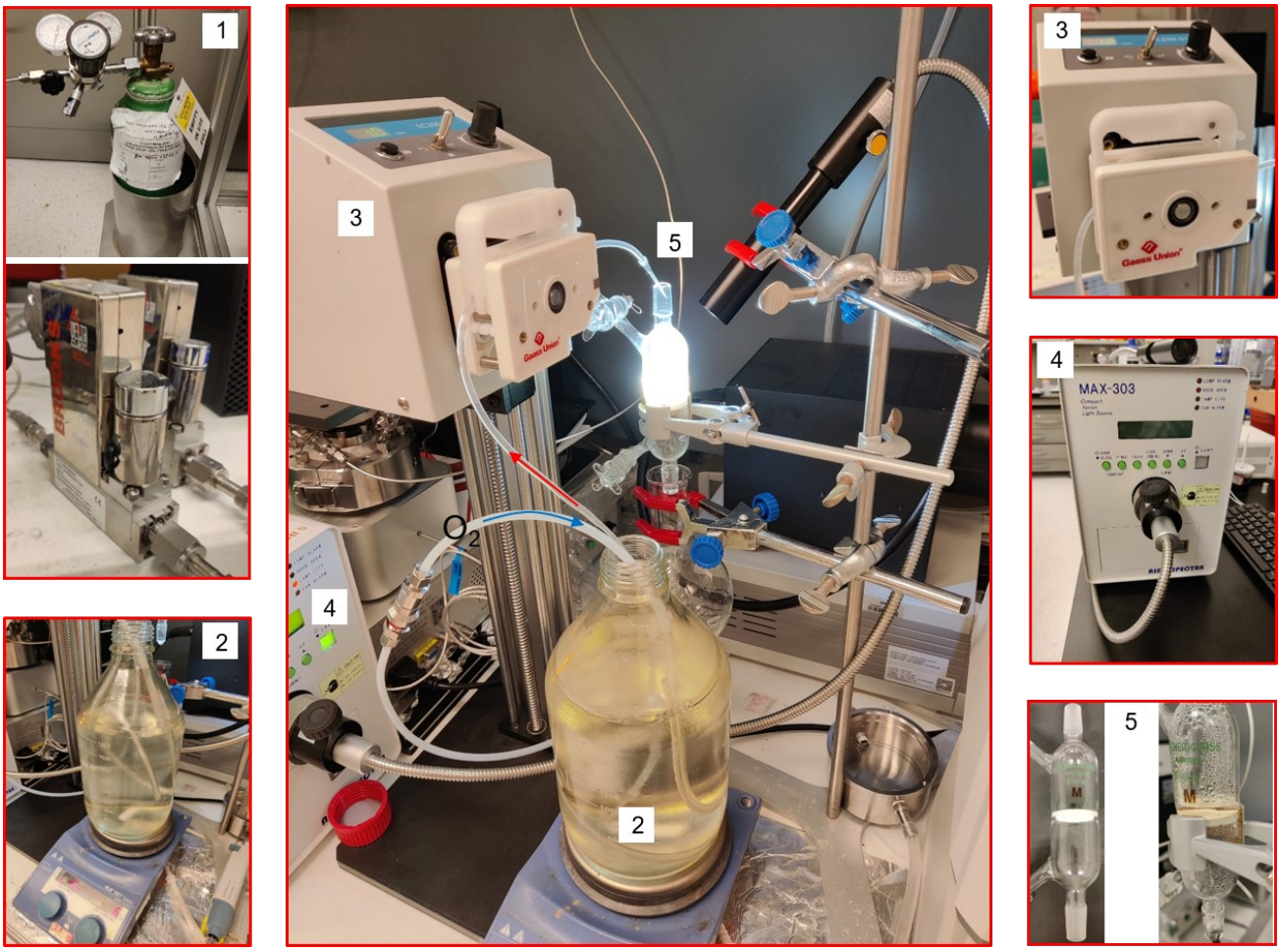

Fig. S23 Overview of the flow reaction system: (1) Gas sources include O_2 cylinders and flow controllers. (2) Continuously pass oxygen into deionized water to maintain oxygen saturation. (3) Peristaltic pump controls feed flow. (4) Xenon lamp with movable fibre optic probe. (5) Quartz reactor with the catalyst bed.

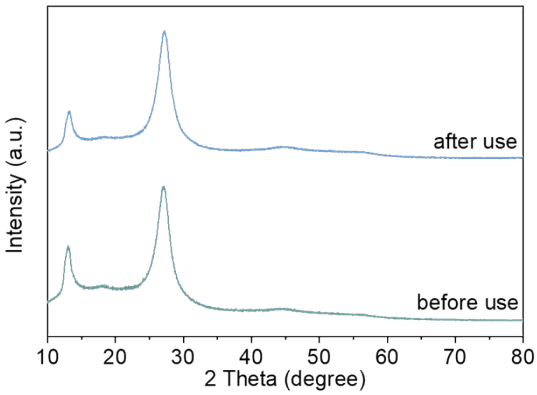

Fig. S24 XRD comparison of prepared CNW03 and CNW03 samples after 4 run use of photoreaction.

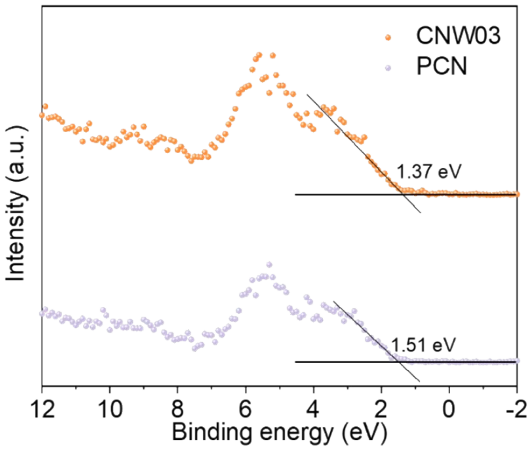

Fig. S25 Valence-band XPS spectra of pristine PCN and CNW03.

The Fermi level of the instrument (VB-XPS) is equilibrated at 4.5 eV utilizing Au metal basis as the reference. In this case, the numerical value of the binding energy in the calibrated VBXPS spectrum is the same as the potential vs. normal hydrogen electrode.

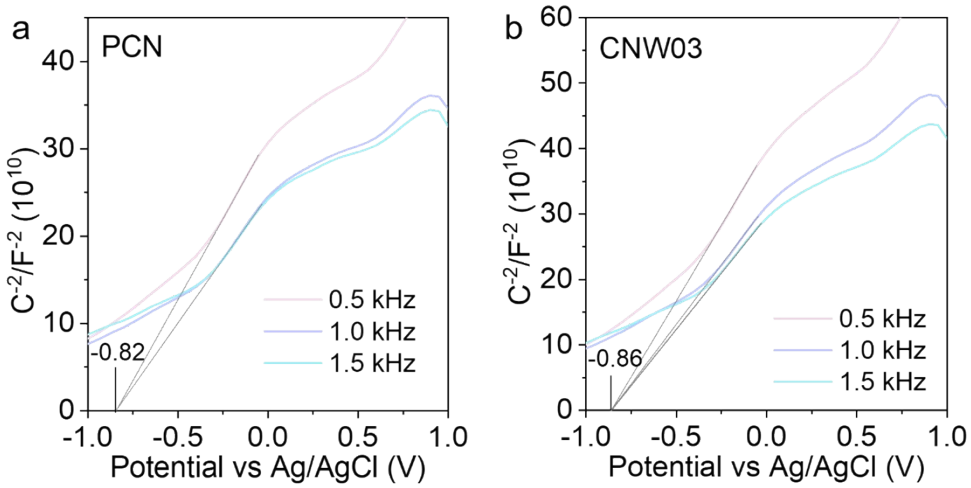

Fig. S26 Mott-Schottky curves of (a) PCN and (b) CNW03 under 0.5, 1.0 and 1.5 kHz.

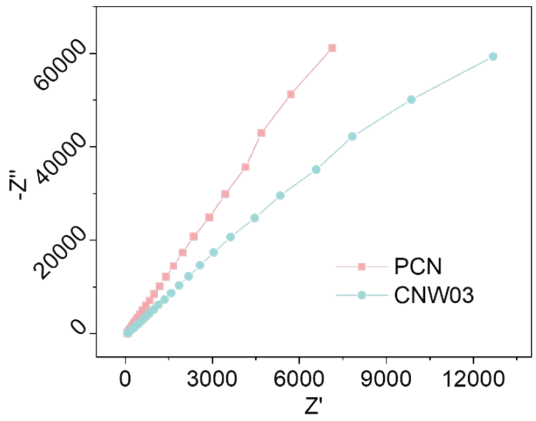

Fig. S27 EIS curves of PCN and CNW03.

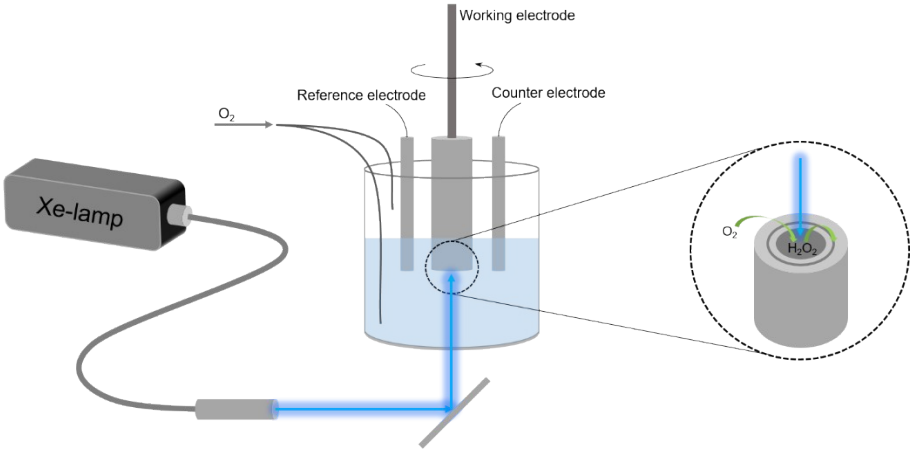

Fig. S28 Schematic diagram of the RRDE experimental setup.

The characterization of photoelectrochemical ORR could not be achieved through the conventional RDE/RRDE station. Thus, a custom-made RDE/RRDE station was needed and designed by integrating with a Xe-lamp, in which the Xe-lamp serves as the light source to excite the photocathode. An optical cable was connected with the Xe-lamp and used to transmit light to the electrode surface. During the reaction, light source from the Xe-lamp vertically illuminated at the rotating electrode, where the photoelectrochemical kinetic information and the formation of peroxide could be obtained.

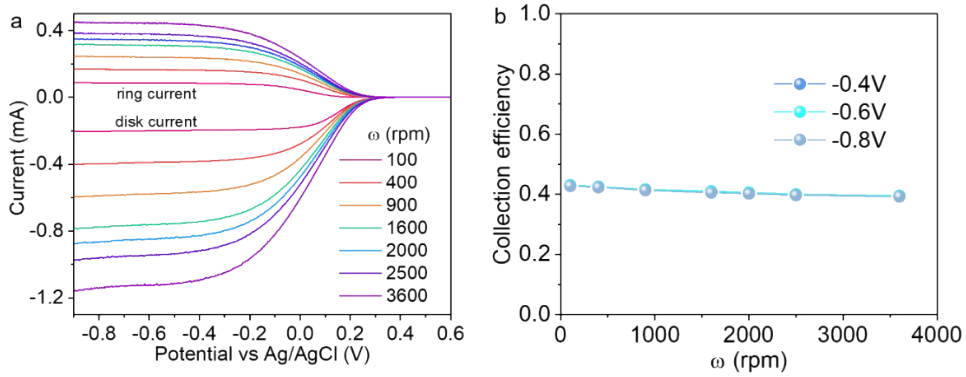

Fig. S29 Determination of correction efficiency of RRDE with $K_3Fe[CN]_6$. a) LSVs of an Ar-saturated aqueous solution of $K_3Fe[CN]_6$ (10 mmol L^{-1}) in the presence of KNO_3 (0.1 M) recorded at a rotating-ring (Pt) and disk (glassy carbon) electrode. b) Plots of collection efficiency at -0.4, -0.6 and -0.8V vs rotation rates.

The collection efficiency (N) was determined to be 0.41.

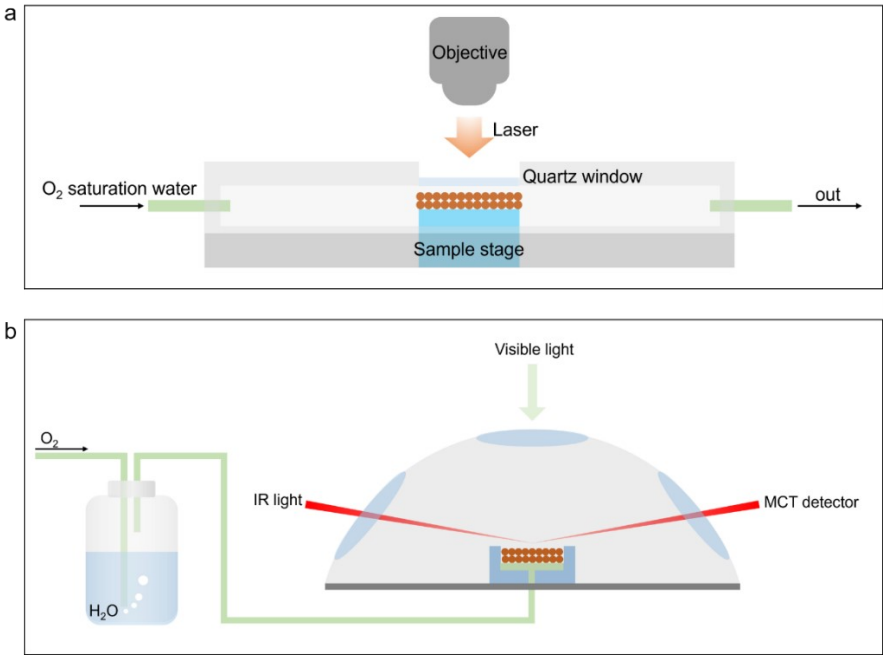

Fig. S30 Schematic diagram of in-situ experiments. (a) Rama test and (b) DRIFTS.

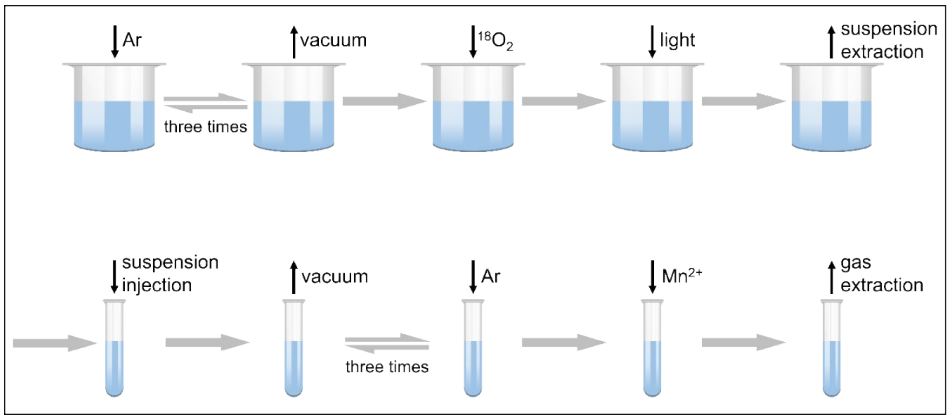

Fig. S31 Schematic diagram showing the isotopic experimental procedure for H_2O_2 production with $^{18}O_2$ and $H_2{}^{16}O$.

Mn^{2+} ions promote the decomposition of H_2O_2 to generate O_2, which is then detected by GCMS.

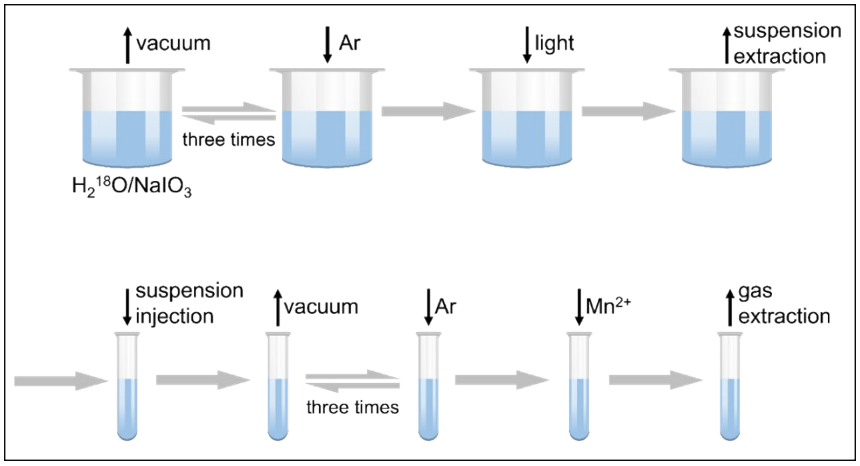

Fig. S32 Schematic diagram showing the isotopic experimental procedure for H_2O_2 production in $H_2{}^{18}O$ with $NaIO_3$ as electron acceptor.

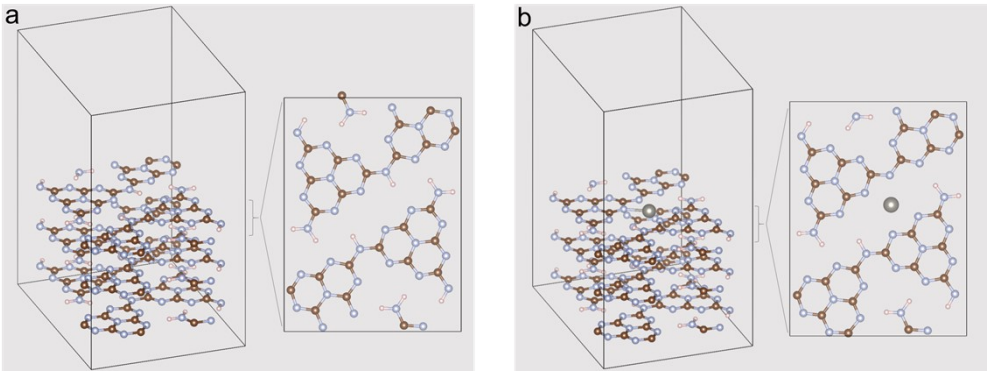

Fig. S33 The fully relaxed model of (a) PCN and (b) CNW.

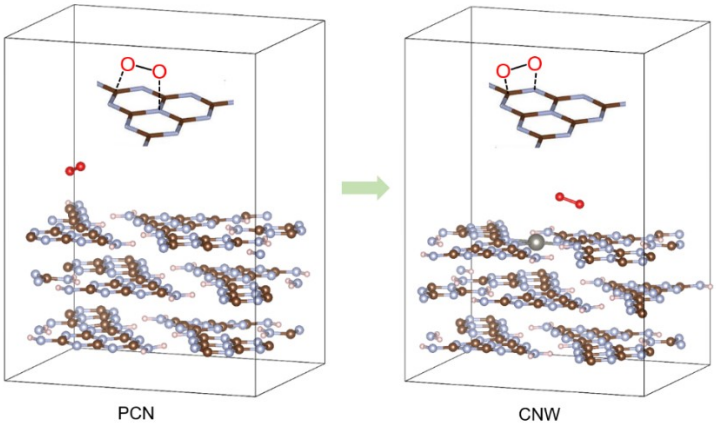

Fig. S34 O_2 adsorption model obtained from DFT calculation before and after loading W isolated atom.

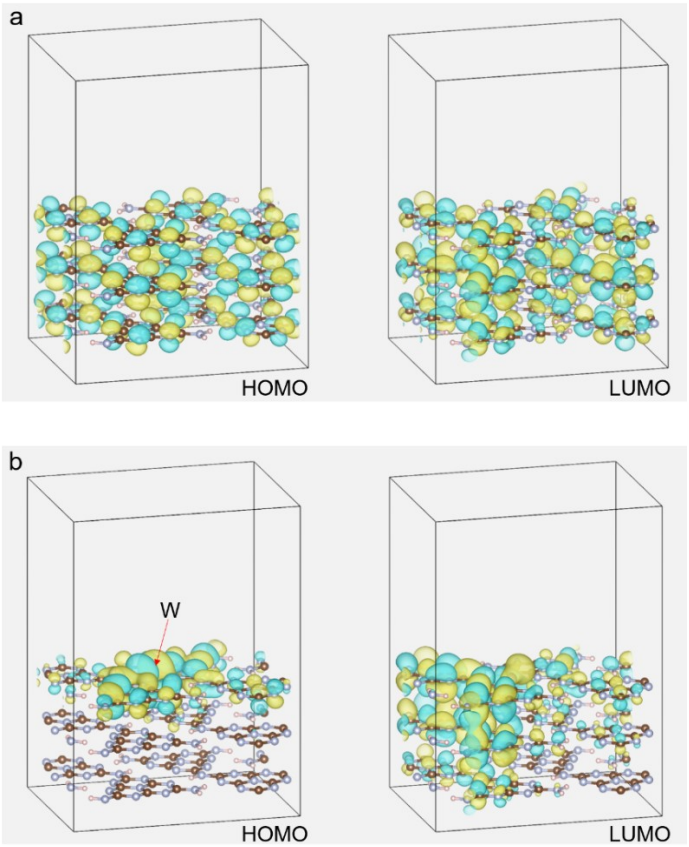

Fig. S35 Band structure calculated by DFT. Distribution of HOMO and LUMO in (a) pristine PCN and (b) CNW.

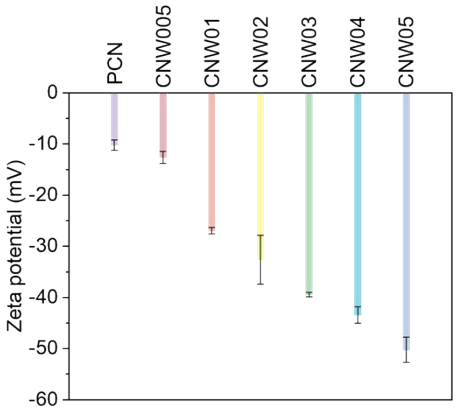

Fig. S36 Zeta potential of prepared catalysts.

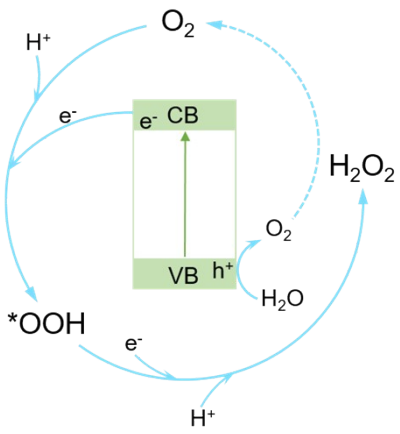

Fig. S37 Proposed mechanism of the overall reaction process over CNW photocatalyst.

Table S1. Fitting results of W L_{III}-edge EXAFS curves.

Sample	Shell	N	R (Å)	σ^2 ($Å^2$)	R factor (%)
W foil	W-W	8	2.72	0.003	0.6
	W-W	6	3.13	0.003	
CNW03	W-N	2.2	2.08	0.003	1.2
	W-N	1.9	2.09	0.003	
	W-C	2.8	2.66	0.003	

Table S2. Comparison of photocatalytic performance in similar systems.

Catalysts	H_2O_2 yield	AOY	SCC	Ref.
Mo:$BiOV_4$	712.5 μmol g^{-1} h^{-1}	5.8%	0.29%	[13]
CNIO-GaSA	331.7 μmol g^{-1} h^{-1}	7.1%	0.4%	[14]
g-C_3N_4/PDI	12.5 μmol g^{-1} h^{-1}	2.6%	0.1%	[15]
$BaTiO_3$:Nb	628 μmol g^{-1} h^{-1}	0.03%	0.14%	[16]
g-C_3N_4/PDI/rGO	24.2 μmol g^{-1} h^{-1}	6.1%	0.2%	[17]
g-C_3N_4/BDI	8.54 μmol g^{-1} h^{-1}	4.6%	0.13%	[18]
Pd/A/$BiVO_4$	805.9 μmol g^{-1} h^{-1}	6.02%	0.25%	[19]
CdS NRs	695.3 μmol g^{-1} h^{-1}	5.8%	0.29%	[20]
g-C_3N_4/PDI-BN-rGO	470 μmol g^{-1} h^{-1}	7.3%	0.27%	[21]
reduced g-C_3N_4	170 μmol g^{-1} h^{-1}	4.3%	0.26%	[22]
g-C_3N_4/MTI	22.9 μmol g^{-1} h^{-1}	5.2%	0.18%	[23]
O/P doped g-C_3N_4	53.8 μmol g^{-1} h^{-1}	2.9%	0.05%	[24]
Py-TPh-COF	167 μmol g^{-1} h^{-1}	2.4%	0.09%	[25]
Nv-C≡N-CN	58 μmol g^{-1} h^{-1}	1.8%	0.23%	[26]
CdS–PDA	255 μmol g^{-1} h^{-1}	6.5%	0.15%	[27]
homo-CN	88.5 μmol g^{-1} h^{-1}	2.6%	0.19%	[28]
Co-CN@G	354.5μmol g^{-1} h^{-1}	9.1%	0.72%	[29]
CNW03	556 μmol g^{-1} h^{-1}	8.53%	0.31%	this work

Table S3. Fitted luminescent decay data for different samples at room temperature.

Sample	τ_1 (ns)	Percent (%)	τ_2 (ns)	Percent (%)	τ_3 (ns)	Percent (%)
PCN	3.38	35.87	17.42	41.92	97.91	22.20
CNW03	0.82	39.44	4.11	41.79	26.71	18.77

The average emission lifetime which reflecting the emission decay process of samples was calculated by the following equation.

$$\tau_a = (A_1\tau_1^2 + A_2\tau_2^2 + A_3\tau_3^2)/(A_1\tau_1 + A_2\tau_2 + A_3\tau_3)$$

where τ_1, τ_2 and τ_3 are the emission lifetime, A_1 and A_2 are the corresponding amplitudes.

References

1. B. Ravel and M. Newville, *J. Synchrotron Radiat.*, 2005, **12**, 537-541.

2. D. Ryoo, X. Xu, Y. Li, J. A. Tang, J. Zhang, P. C. Van Zijl and G. Liu, *Anal. Chem.*, 2017, **89**, 7758-7764.

3. Z. Wei, M. Liu, Z. Zhang, W. Yao, H. Tan and Y. Zhu, *Energy Environ. Sci.*, 2018, **11**, 2581-2589.

4. K. Jiang, S. Back, A. J. Akey, C. Xia, Y. Hu, W. Liang, D. Schaak, E. Stavitski, J. K. Nørskov, S. Siahrostami and H. Wang, *Nat. Commun.*, 2019, **10**, 3997.

5. J. VandeVondele, M. Krack, F. Mohamed, M. Parrinello, T. Chassaing and J. Hutter, *Comput. Phys. Commun.*, 2005, **167**, 103-128.

6. S. Goedecker, M. Teter and J. Hutter, *Phys. Rev. B*, 1996, **54**, 1703.

7. C. Hartwigsen, S. Gœdecker and J. Hutter, *Phys. Rev. B*, 1998, **58**, 3641.

8. A. Heyden, A. T. Bell and F. J. Keil, *J. Chem. Phys.*, 2005, **123**, 224101.

9. J. VandeVondele and J. Hutter, *J. Chem. Phys.*, 2007, **127**, 114105.

10. J. P. Perdew, K. Burke and M. Ernzerhof, *Phys. Rev. Letters*, 1996, **77**, 3865.

11. S. Grimme, J. Antony, S. Ehrlich and H. Krieg, *J. Chem. Phys.*, 2010, **132**, 154104.

12. T. Lu and F. Chen, *J. Comput. Chem.*, 2012, **33**, 580-592.

13. T. Liu, Z. Pan, J. J. M. Vequizo, K. Kato, B. Wu, A. Yamakata, K. Katayama, B. Chen, C. Chu and K. Domen, *Nat. Commun.*, 2022, **13**, 1034.

14. H. Tan, P. Zhou, M. Liu, Q. Zhang, F. Liu, H. Guo, Y. Zhou, Y. Chen, L. Zeng and L. Gu, *Nat. Synth.*, 2023, DOI: 10.1038/s44160-023-00272-z, 1-7.

15. Y. Shiraishi, S. Kanazawa, Y. Kofuji, H. Sakamoto, S. Ichikawa, S. Tanaka and T. Hirai, *Angew. Chem. Int. Ed.*, 2014, **53**, 13454-13459.

16. X. Zhou, F. Yan, A. Lyubartsev, B. Shen, J. Zhai, J. C. Conesa and N. Hedin, *Adv. Sci.*, 2022, **9**, 2105792.

17. Y. Kofuji, Y. Isobe, Y. Shiraishi, H. Sakamoto, S. Tanaka, S. Ichikawa and T. Hirai, *J. Am. Chem. Soc.*, 2016, **138**, 10019-10025.

18. Y. Kofuji, S. Ohkita, Y. Shiraishi, H. Sakamoto, S. Tanaka, S. Ichikawa and T. Hirai, *ACS Catal.*, 2016, **6**, 7021-7029.

19. M. Sun, X. Wang, Y. Li, H. Pan, M. Murugananthan, Y. Han, J. Wu, M. Zhang, Y. Zhang and Z. Kang, *ACS Catal.*, 2022, **12**, 2138-2149.

20. Y. Zhang, L. Wang, H. Huang, C. Hu, X. Zhang, C. Wang and Y. Zhang, *Appl. Catal. B: Environ.*, 2023, **331**, 122714.

21. Y. Kofuji, Y. Isobe, Y. Shiraishi, H. Sakamoto, S. Ichikawa, S. Tanaka and T. Hirai, *ChemCatChem*, 2018, **10**, 2070-2077.

22. Z. Zhu, H. Pan, M. Murugananthan, J. Gong and Y. Zhang, *Appl. Catal. B: Environ.*, 2018, **232**, 19-25.

23. Y. Kofuji, S. Ohkita, Y. Shiraishi, H. Sakamoto, S. Ichikawa, S. Tanaka and T. Hirai, *ACS Sustainable Chem. Eng.*, 2017, **5**, 6478-6485.

24. H. Kim, K. Shim, K. E. Lee, J. W. Han, Y. Zhu and W. Choi, *Appl. Catal. B: Environ.*, 2021, **299**, 120666.

25. J. Sun, H. S. Jena, C. Krishnaraj, K. Singh Rawat, S. Abednatanzi, J. Chakraborty, A. Laemont, W. Liu, H. Chen and Y.-Y. Liu, *Angew. Chem. Int. Ed.*, 2023, **62**, e202216719.

26. X. Zhang, P. Ma, C. Wang, L. Gan, X. Chen, P. Zhang, Y. Wang, H. Li, L. Wang and X. Zhou, *Energy Environ. Sci.*, 2022, **15**, 830-842.

27. Z. Wei, S. Zhao, W. Li, X. Zhao, C. Chen, D. L. Phillips, Y. Zhu and W. Choi, *ACS Catal.*, 2022, **12**, 11436-11443.

28. Q. Chen, C. Lu, B. Ping, G. Li, J. Chen, Z. Sun, Y. Zhang, Q. Ruan and L. Tao, *Appl. Catal. B: Environ.*, 2023, **324**, 122216.

29. W. Wang, Q. Song, Q. Luo, L. Li, X. Huo, S. Chen, J. Li, Y. Li, S. Shi and Y. Yuan, *Nat. Commun.*, 2023, **14**, 2493.